The Meso-NH Atmospheric Simulation System:

Scientific Documentation

Part V: Budget and Diagnostics

Acknowledgments

This volume contains contributions from P. Bechtold, S. Belair, Ph. Bougeault, J.M. Carrière, J. Cuxart, V. Ducrocq, C. Fischer, M. Georgelin, P. Héreil, J.-P. Lafore, C. Liousse, C. Mari, I. Mallet, P. J. Mascart, V. Masson, J.-P. Pinty, E. Richard, K. Suhre, J. Stein, P. Tulet, and J. Vilà-Guerau de Arellano. As editors, we would like to express our deep appreciation for the dedicated work of all contributors. The Meso-NH project is the achievement of a much larger team. Our thanks extend to all those who are not cited here, but have given their best to create this unique tool.

Philippe Bougeault and Patrick Mascart

Since the 2002 edition, in addition to the contributors cited above, thanks have to be extended to C. Augros, F. Auguste, D. Barbary, C. Barthe, S. Berthet, Y. Bouteloup, C. Bovalo, O. Caumont, J.-P. Chaboureau, M. Chong, A. Costes, F. Couvreux, T. Dauhut, G. Delautier, J. Escobar, O. Geoffroy, P.A. Joulin, C. Lac, P. Le Moigne, M. Leriche, Q. Libois, T. Lunet, M. Mandement, T. Marić, G. Molinié, T. Nagel, J., O. Nuissier, Pergaud, D. Ricard, Q. Rodier, R. Schoetter, F. Solmon, O. Thouron, M. Tomasini, B. Tsenova, B. Vié and F. Visentin.

Jean-Pierre Chaboureau

Chapter 1

Budget Analysis

Contents

1.1 Introduction

The budget analysis is a major component of the **comprehensive physical package** offered by the Meso-NH Atmospheric Simulation System. This analysis is performed in three steps.

1. In-line computation of the budget for all prognostic variables of the model. The results are written on a diachronic MNH file.
2. The results are written on a diachronic MNH file.
3. Finally the graphical package reads these files, and visualizes the results.

The budget analysis has been designed to be easily performed. The user has to prescribe variables for which he wants a budget, processes to store, and spatio-temporal domain type and characteristics, on which the budgets are computed. For simulations with several nested models, the budget analysis has been limited to only one model.

1.2 Budget definition

1.2.1 Equations

The budget analysis is based on the model equations written in flux form, discretized on the computational grid (see chapter on discretization in Part I). For instance for a prognostic variable α, we have the following generic equation;

$$\frac{\partial}{\partial t}(\tilde{\rho}\alpha) \;=\; -\frac{\partial}{\partial \overline{x}}(\tilde{\rho}U^c\,\alpha) \;-\; \frac{\partial}{\partial \overline{y}}(\tilde{\rho}V^c\,\alpha) \;-\; \frac{\partial}{\partial \overline{z}}(\tilde{\rho}W^c\,\alpha) \;+\; \sum_{p=4}^{p_{max}} \mathcal{S}\alpha_p \tag{1.1}$$

where $\mathcal{S}\alpha_p$ represents the α source due to the p^{th} process. The first 3 terms of the r.h.s. of this equation ($i.e.\ p = 1$, 2 and 3) correspond to the advection contributions in the $\overline{x}$, $\overline{y}$ and $\overline{z}$-directions respectively. The budget analysis simply consists in storing all the sources terms, necessary to explain the temporal evolution of the α variable. To check the budget closure, and to physically understand it, it is necessary to add the storage of variable α at the initial and final instant of the budget, and of its mean value for this time period.
At this point, it is important to note that the budget is not performed for the physical variable α, but for $\tilde{\rho}\alpha$ (with $\tilde{\rho} = \rho_{dref}J$), i.e. the quantity multiplied by the mass of dry air contained in the grid box volume. The flux form of the advection equation, allows the conservation properties of the transport process to be exactly accounted for.

1.2.2 Average operators

Such budget analysis quickly generates a huge amount of information, difficult to handle and to physically understand. Thus in practice, the budgets terms can be conveniently compressed in different ways, by applying the following operator:

$$\frac{1}{t_2 - t_1}\sum_{t=t_1}^{t_2}\sum_{i}\sum_{j}\sum_{k}\,\mathcal{P}^t_{i,j,k}\,\Delta\overline{x}\,\Delta\overline{y}\,\Delta\overline{z}\,\Delta t \tag{1.2}$$

where $\mathcal{P}$ is for a given process.

1. Several **processes** can be added to form a single process. For example the summation of the 3 first processes of Eq. 1, corresponds to the total advection.

2. The **temporal average** $\frac{1}{t_2 - t_1}\sum_{t=t_1}^{t_2}\Delta t$ of the budgets on a time interval (t_1 to t_2) longer than a time step, allows to obtain more significant results for system presenting high temporal fluctuations.

3. The **vertical integration** of the budgets allows understandng of the behaviour of a column of atmosphere for a given layer (k_1 to k_2). It corresponds to the operator $\sum_{k=k_1}^{k_2}\Delta\overline{z}$.

4. The **”horizontal” integration** (performed on the computational levels) gives significant information for given horizontal subdomain. It can be performed for 2 types of subdomain; either a cartesian zone, or a complex area defined by a mask.

- **Cartesian domain**

  In that case the user defines a cartesian sub-domain, where the budget will be performed, by setting the horizontal coordinates of the edges of this zone (i_1 to i_2 and j_1 to j_2). The horizontal average operator is:

$$\sum_{i=i_1}^{i_2}\sum_{j=j_1}^{j_2}\Delta\overline{x}\,\Delta\overline{y} \tag{1.3}$$

The budget can be compressed or not in the 2 horizontal directions. In case of no compression, the resulting budget fields are 3D over the selected cartesian horizontal zone, whereas 1D budget for this zone is returned in case of total compression. For some systems characterized by a strong slab symmetric structure (fronts, convection line,...), a compression in the along-system direction results in 2D budget fields, well adapted to analyze them.

- **Defined by a mask**

  For a wide range of systems, it is convenient to analyze budgets over complex zones, which can temporally evolve. For example a cloud population simulation can be analyzed, by considering zones with precipitation, and/or clear air regions... In that case, the user must define the differents zones, owing to a set of horizontal masks ($mask(i,j)$), refreshed every time step if necessary. The budgets are horizontally averaged in each zone, so that 1D vertical budget profiles are provided. Thus, the horizontal integration operator is:

$$\sum_{mask\,(i,j)} \Delta\overline{x}\,\Delta\overline{y} \tag{1.4}$$

NB: In the case of non-flat topography, the budget compression by the above horizontal operators, results in budgets over volumes following the non-horizontal computational levels. Thus to obtain budget over horizontal boxes having a physical meaning, spatial interpolations must be performed before compression. As a consequence, in case of flow over topography, the best is to avoid the horizontal compression. The interpolation and the compression will be therefore performed by the post-processing programs.

Chapter 2

Diagnostics

Contents

2.1 Some formulae

Temperature

The temperature `TEMP` (°C) is computed as:

$$T = \Pi\theta - T_t \tag{2.1}$$

where T_t is the temperature of the triple point.

Vapor pressure and relative humidity

The vapor pressure (`VPRES`) is computed as:

$$e = \frac{P}{1 + r_v\, R_d/R_v} \tag{2.2}$$

The relative humidity (`REHU`) is computed as:

$$Hu = \frac{e}{e_s(T)} \tag{2.3}$$

When a mixed microphysical scheme is activated during the simulation, the saturation vapor pressure $e_s(T)$ is computed over ice at points where temperature is below the triple point.

Refraction coindexes

Following Hill et al. (1980) the refraction coindex (`COREF`) is computed as:

$$N = (77.6/T) \times (P + 4810\, e/T) - 6e/T \tag{2.4}$$

where P and e are in hPa.
The modified refraction coindex (`MCOREF`) is computed as:

$$M = N + Z\, 10^6 a \tag{2.5}$$

where Z and a are respectively the altitude and the Earth radius in m.

Virtual potential temperature

The virtual potential temperature (`THETAV`) is given by:

$$\theta_v \quad = \quad \theta \times \frac{(1+r_v R_v/R_d)}{(1+r_w)} \tag{2.6}$$

where r_w is the mixing ratio of total water substance

$$r_w \quad = \quad r_v + r_c + r_r + r_i + r_s + r_g + r_h$$

Equivalent potential temperature

The formulation of the equivalent potential temperature (`THETAE`) is taken from Bolton (1980) following its equations (16), (21) and (43):

$$\begin{aligned} \theta_e &= \theta \ \exp\left[\Big(\frac{3376}{T_L} - 2.54\Big)\, r_v\,(1+0.81 r_v)\right] \qquad (2.7)\\ \text{where } T_L &= \frac{2840}{3.5\ln T - \ln e - 4.805} + 55 \\ \text{and } e &= \frac{0.01\,P\,r_v}{0.622 + r_v} \end{aligned}$$

Vorticity quantities

The relative vorticity (`UM1,VM1,WM1`) is computed as:

$$\begin{aligned} \boldsymbol{\zeta} = \boldsymbol{\nabla} \wedge \boldsymbol{U} \quad &= \quad (\frac{\partial w}{\partial \hat{y}} - \frac{\partial v}{\partial \hat{z}})\boldsymbol{i} \\ &\quad +(\frac{\partial u}{\partial \hat{z}} - \frac{\partial w}{\partial \hat{x}})\boldsymbol{j} \\ &\quad +(\frac{\partial v}{\partial \hat{x}} - \frac{\partial u}{\partial \hat{y}})\boldsymbol{k} \qquad (2.8) \end{aligned}$$

The absolute vorticity (`ABVOR`) takes into account the rotation of the earth:

$$\xi = \boldsymbol{\zeta}.\boldsymbol{k} + 2\Omega\sin\varphi \tag{2.9}$$

Potential vorticity

The Ertel potential vorticity (`POVOM`) is computed as:

$$P = \frac{\boldsymbol{\zeta}.\boldsymbol{\nabla}(\theta)}{\rho_{dref}} \tag{2.10}$$

The unit is the Potentiel Vorticity Unit, 1 PVU= 10^6 K m^2 kg^{-1} s^{-1}

Moist potential vorticities

The virtual potential vorticity (`POVOV`) is

$$P_v = \frac{\boldsymbol{\zeta}.\boldsymbol{\nabla}(\theta_v)}{\rho_{dref}} \tag{2.11}$$

and the equivalent virtual potential vorticity (`POVOE`)

$$P_e = \frac{\boldsymbol{\zeta}.\boldsymbol{\nabla}(\theta_e)}{\rho_{dref}} \tag{2.12}$$

Geostrophic and ageostrophic winds

With the LHE system (see Chapter Basic Equations in Part I), the geostrophic wind (`UM88`,`VM88`, `UM89`,`VM89`) is computed as:

$$u_g = -\frac{1}{f}\frac{\partial(C_{pd}\theta_{vref}\Pi')}{\partial\hat{y}} \quad ; \quad v_g = \frac{1}{f}\frac{\partial(C_{pd}\theta_{vref}\Pi')}{\partial\hat{x}} \tag{2.13}$$

With the MAE and DUR systems (see book1, chapter 2), the geostrophic wind is computed as:

$$u_g = -\frac{1}{f}\,C_{pd}\theta_{vref}\,\frac{\partial\Pi'}{\partial\hat{y}} \quad ; \quad v_g = \frac{1}{f}\,C_{pd}\theta_{vref}\,\frac{\partial\Pi'}{\partial\hat{x}} \tag{2.14}$$

where

$$\Pi' = \left(\frac{P}{P_{00}}\right)^{\frac{R_d}{C_{pd}}} - \Pi_{ref}$$

The ageostrophic wind is computed as:

$$u_{ag} = u - u_g \quad ; \quad v_{ag} = v - v_g$$

Near-surface wind

Zonal and meridional wind at 10 m height above ground level (AGL), $u_{10\mathrm{m}}, v_{10\mathrm{m}}$ are stored in variables `UM10`, `VM10` and computed as:

- If first physical vertical mass level `XZHATM(IKB)` is below 10 m height AGL (i.e. the level 10 m is between two physical vertical levels of the grid), with `IKB`= 1 + `JPVEXT`, the index of this level, then at mass level z_i = `XZHATM(`i`)` at which `XZHATM(`i`)` $\leq 10\,\mathrm{m} <$ `XZHATM(`$i+1$`)`, a linear interpolation of u_i and u_{i+1} is performed:

$$\frac{u_{10\mathrm{m}} - u_i}{u_{i+1} - u_i} = \frac{10 - z_i}{z_{i+1} - z_i} \tag{2.15}$$

$$\Rightarrow \quad u_{10\mathrm{m}} = u_i + (u_{i+1} - u_i)\frac{10 - z_i}{z_{i+1} - z_i} \tag{2.16}$$

  and similarly,

$$v_{10\mathrm{m}} = v_i + (v_{i+1} - v_i)\frac{10 - z_i}{z_{i+1} - z_i} \tag{2.17}$$

- If `XZHATM(IKB)` is above 10 m height AGL:
  - if $\texttt{N2M} = 0$ in `NAM_DIAG_SURFn`, `UM10` and `VM10` are not computed (equal to `ZUNDEF`)
  - if $\texttt{N2M} > 0$ in `NAM_DIAG_SURFn`, `UM10` and `VM10` are initialized by SURFEX model diagnostic variables `ZON10M`, `MER10M`:

$$u_{10\mathrm{m}} = \texttt{ZON10M} \tag{2.18}$$

$$v_{10\mathrm{m}} = \texttt{MER10M} \tag{2.19}$$

Three formulae are available for wind gusts at 10 m height AGL. As a reminder, the World Meteorological Organization (WMO, 2021) defines wind gusts as the maximum value, over the observing cycle, of the 3-second running average wind speed (gust duration of 3 s,). Currently, in France, this variable, called ”FXI3S” is only provided in a limited number of observation reports (e.g., METAR) and for a limited number of Météo-France weather stations (e.g. stations located on airports). In most reports (SYNOP, RADOMEH, RADOME1M, etc.), the variable provided is the maximum instantaneous wind speed (”FXI”) which is the maximum value, over the observing cycle, of all the observations, which are made at periods varying between 0.25 s and 0.5 s depending on the anemometer technology and model (cup, ultrasonic or propeller). Coefficients (3.8 or 4, see below) may have been set to model FXI and they may need to be adapted to model FXI3S.

$$\texttt{FF10MAX} = \sqrt{u_{10\mathrm{m}}^2 + v_{10\mathrm{m}}^2} + 4\sqrt{\mathrm{TKE}_{\mathrm{IKB}}} \tag{2.20}$$

$$\texttt{FF10MAX2} = \sqrt{u_{10\mathrm{m}}^2 + v_{10\mathrm{m}}^2} + 4\sqrt{\mathrm{TKE}_{10\mathrm{m}}} \tag{2.21}$$

$$\texttt{FF10MAX\_AROME} = \sqrt{u_{10\mathrm{m}}^2 + v_{10\mathrm{m}}^2} + 3.8\sqrt{\mathrm{TKE}_{20\mathrm{m}}} \tag{2.22}$$

- If `XZHATM(IKB)` is below 10 m height AGL: `FF10MAX`, `FF10MAX2` and `FF10MAX_AROME` are computed according to Eqs. 2.20–2.22.
- If `XZHATM(IKB)` is above 10 m height AGL:
  - if $\texttt{N2M} = 0$ in `NAM_DIAG_SURFn`: `FF10MAX`, `FF10MAX2` and `FF10MAX_AROME` are not computed.
  - if $\texttt{N2M} > 0$ in `NAM_DIAG_SURFn`: `FF10MAX` is computed with $u_{10\mathrm{m}}$ and $v_{10\mathrm{m}}$ given by SURFEX as in Eqs 2.18–2.19. `FF10MAX_AROME` is computed only if `XZHATM(IKB)` is below 20 m height AGL. `FF10MAX2` is not computed.

These formulations are inspired by Brasseur (2001). `FF10MAX2` formula was added to reduce the sensitivity to `IKB` and therefore the first vertical level of the grid. `FF10MAX_AROME` corresponds to the formulation in AROME-France cy46t1 (operational in 2024) which is controlled by the namelist ”NAMPHY2” and the parameters ”FACRAF” and ”HTKERAF” in AROME code. Computation is done in ”accldia.f90”.
In addition to these variables providing the wind gust at the exact time of the output diachronic file: the maximum between two diachronic files is provided by `FF10MAX_MA`, `FF10MAX2_MA` and `FF10MAX_AROME_MA` when `NAM_MEAN LMEAN_FIELD=T` in `EXSEG$n.nam` file. These maxima are provided only if `XZHATM(IKB)` is below 10 m height AGL (no call to SURFEX).

Mean sea level pressure

The surface pressure (`MSLP`) is first computed as the mean between the pressure at the first mass level and at the level below. Then it is reduced to the mean sea level (where the height is zero) following the Laplace law:

$$P_{sea} = P_{surf}\ \exp\left(\frac{g z_{surf}}{R_d . T_v^m}\right) \tag{2.23}$$

where z_{surf} is the orography and T_v^m is the mean virtual temperature between the ground level and the sea level (the latter is extrapolated from the first with a climatological gradient of $-6.5K/km$).

Thickness of water species

The thickness of a water specy x (`THVW, THCW, THRW, THIC, THSN, THGR, THHA`) (with $x = v, c, r, i, s, g$ or h) is computed as:

$$\sum_{k=k_B}^{k=k_E} \frac{\rho_{dref}}{\rho_{liq.w.}}\, r_x(k)\, \Delta z_k \tag{2.24}$$

Height of explicit cloud top

For every columns scanned from the model top to the bottom, the height of explicit cloud top (`HEC`) is the height where the cloud mixing ratio (r_c) exceeds the value of 0.1 g/kg. If a mixed microphysical scheme is activated during the simulation, the ice mixing ratio (r_i) is also taken into account (with the same threshold), and the height is the higher between the one of the top determined with r_c and the top determined with r_i.

Height and temperature of maximum cloud top

If a convection scheme is activated during the simulation and if you ask for convective diagnostics (`NCONV_KF≥0`), the top of convective cloud computed by the convection scheme is compared to the previous one of explicit cloud in every columns. The height and the temperature of the higher top (`HC, TC`) are deduced. For clear-sky columns, the height is 0 and the temperature is the one of the ground.

Visibility

The visibility (`VISI`), function of the liquid water content, has not an universal formula. It is computed here for low level clouds according to Kunkel (1984) and the COBEL model:

$$VISI = \frac{3.9}{144.7(\frac{\rho_{dref} r_c}{1.+r_c})^{0.88}} \tag{2.25}$$

Height and index of boundary layer top

The boundary layer top (`HBLTOP, KBLTOP`) is found by checking $\partial\theta_v/\partial z$, and comparing it to the gradient between 5000 m of height and the ground. It is the same algorithm than in PREP_REAL_CASE (used to shift variables when changing vertical grid), which has been found to work fairly well from polar to saharian area. More details can be found in the routine *free_atm_profile.f90* itself.

Convective diagnostics

The convective instability of an atmospheric layer can be described using a series of diagnostics: CAPE (Convective Available Potential Energy), CIN (Convective Inhibition), DCAPE (Downdraft CAPE), and DCIN (Downdraft CIN). All these parameters evaluate the buoyancy of a parcel displaced a finite distance (rising in case of updraft or sinking in case of downdraft) under a reversible or pseudoadiabatic process. They are computed following the code of Emanuel (1994).
In a conditionally unstable atmosphere, the potentially unstable parcels will be generally be negatively buoyant in the lower part of the sounding before becoming positively buoyant above their Level of Free Convection (LFC). CIN defines the potential energy needed to lift a parcel to its LFC while CAPE is the amount of energy available for the convection of a parcel lifted from its LFC to its Level of Neutral Buoyancy (LNB).

$$\text{CIN} = -\int_{i}^{LFC} R_d(T_{vp} - T_{ve})\, dz \tag{2.26}$$

$$\text{CAPE} = \int_{LFC}^{LNB} R_d(T_{vp} - T_{ve})\, dz \tag{2.27}$$

where T_{vp} and T_{ve} are the virtual temperature of the lifted parcel and of the environment, respectively. Conversely, DCAPE and DCIN are the positive and negative parts of buoyant energy in the downdrafts, respectively.

2.2 Conditional sampling

A new Large-Eddy Simulation (LES) diagnostic is proposed based on different idealised tracers. This conditional sampling is based on the combination of passive tracers and thermodynamic variables in order to characterize organized structures in cloud-free and cloudy boundary layers. For a complete documentation, please refer to Couvreux et al. (2010). A maximum of three tracers can be activated.
The first scalar is emitted with a constant flux at the surface. The second one is emitted in the layer just below cloud base (z_b-150m – z_b-50m) if ever clouds exist; the third one is emitted in the layer just above cloud top (z_t+50m – z_t+150m) if ever clouds exist; z_b and z_t being respectively cloud base and cloud top. All scalars undergo a radioactive decay with a time constant τ that can be adjusted by the user (the default value is 15 min):

$$\frac{\partial C}{\partial t} = -\frac{C}{\tau} \tag{2.28}$$

The conditional sampling selects all the grid points that follows the conditions:

$$x \in CS \text{ if } C^{'}(x, y, z) > m \times \max(\sigma_C(z), \sigma_{min}(z)) \text{ and } w^{'} > 0 \tag{2.29}$$

m is a scaling factor that can be adjusted by the user (the default value is 1), $\sigma_C(z)$ is the standard deviation of C at the altitude z and σ_{min} is a minimum threshold defined as:

$$\sigma_{min}(z) = 0.05 \times \frac{1}{z}\int_0^z \sigma_C(k)dk \tag{2.30}$$

It corresponds to 5% of the average standard deviation at lower levels and ensures that no point is selected in a non-turbulent environment. In case of cumulus-topped thermals, this definition is applied up to $z = z_b + (z_t - z_b)/4$. Above that level, a cloud condition ($q_l > 0$, with q_l being the liquid water content) is added in order to select only cloudy grid points and no air detrained from the cloud. This is done independently at each vertical level.

This sampling is able to characterize thermals from the surface to the top of the dry or cloudy boundary layers. It therefore characterizes the bottom-up transport.

This diagnostic is activated using the namelist NAM_COND_SAMP with the following keys: LCONDSAMP a flag to activate the sampling, NCONDSAMP the number of used conditional sampling, XRADIO the period of radioactive decay, and XSCAL the scaling factor.

2.3 Coarse-graining techniques

Coarse-graining techniques calculate the average and standard deviation of any model field over a set of user-defined blocks. Such techniques are useful when developing a subgrid parameterization and are commonly applied to a set of two simulations that differ only in their resolution. The high-resolution simulation provides the average fields on a coarse grid that should be obtained by the low-resolution simulation run with the subgrid parameterization to be tested. The operator is a parallel algorithm that can easily be employed over large grids. The operator can also calculate a moving average over a user-defined block. Both the grid scale and the subgrid scale of any field can therefore be estimated (Dauhut et al. 2016).

2.4 Three-dimensional clustering

A clustering operator is available to identify any object or coherent structure and to characterize them in terms of their geometrical, thermodynamical, and dynamical properties. This technique was developed by Dauhut et al. (2016) to identify the few updrafts of “Hector the Convector” in the Northern Territory of Australia from among the more than 16 000 updrafts that hydrate the stratosphere. Updrafts were defined as three-dimensional objects made of connected grid points for which the vertical velocity exceeded an arbitrary threshold. Two grid points sharing a common face either in the horizontal or vertical direction were considered connected, while diagonal connections were considered only in the vertical direction. This technique has also been used for the attribution of dust emission, defined as surface objects, to wind regimes (Chaboureau et al. 2016).

Three 3D fields are generated. CLUSTERID is an identity number, CLUSTERLV is the level where the object has been identified for the first time (at its bottom if LBOTUP is true, at its top otherwise), CLDSIZE is the horizontal section of the object at the current level. Together, CLUSTERID **and** CLUSTERLV refer univoqually to a unique 3D object. Their value is homogeneous inside each identified object. CLOUDSIZE is homogeneous at each level inside each object.

In principle, the algorithm does first a 2D clustering at each level. Then the identification is propagated on the vertical direction: for each cluster at the current level CLUSTERID and CLUSTERLV values are changed if a connected cluster was identified at the previous level (i.e. just below if LBOTUP is true, or just above otherwise). For the cases where various 2D clusters where identified at the previous level, then the priority is given to the cluster with the largest section at the previous level, i.e. its CLUSTERID and CLUSTERLV are attributed to the current cluster. In case of further conflict, arbitrary choices are made.

The user is free to change the 3D field used for detection, the threshold value for detection and the direction of propagation of the identification. Dauhut et al. (2016) investigated the updrafts using a 10 m s^{-1} threshold on the vertical velocity field w and propagating the identification from the bottom to the top. Another study investigated the overshoots using a 10 $^{-5}$ kg kg^{-1} on the cloud field (sum of snow, graupel, liquid and ice cloud mixing ratios) and propagating the identification from the top to the bottom. The developer can further implement the possibility to consider other fields for the detection of the 3D objects. As with any clustering algorithm, a too low threshold value could lead to overconnected regions.

2.5 Kinetic energy spectra

Observational studies (Nastrom and Gage 1985; Lindborg 1999) have shown that the kinetic energy (KE) spectra follow a k^{-3} dependence in the large scales (where k is the wavenumber) dominated by rotational modes and a transition to a shallower k$^{-5/3}$ dependence in the mesoscale and smaller scales, dominated by divergent modes.

Spectral analysis is a powerful tool to assess how the KE is distributed in atmospheric models according to spatial scales and their capacity to reproduce observational spectra (Koshyk et al. 1999). In particular, Skamarock (2004) used spectral analysis to define the effective resolution of the WRF model, i.e. the scale from which the model departs from the theoretical slope, also given by a simulation with a finer grid spacing. Indeed, a part of small-scale energy is damped as it is affected by implicit and explicit diffusion, the tail of spectra showing a rapid decrease of KE.

An algorithm of spectra computation has been coded for Meso-NH (Ricard et al. 2013), based on Denis et al. (2002) study, which used a discrete cosine transform (DCT) (Ahmed and Rao 1974) to convert grid-point fields into spectral ones. Indeed, spectra computation from a discrete cosine transform is particularly well adapted for limited-area models to overcome the problem of non-periodic domain. Unlike spectra computation based on FFT, the meteorological fields do not need any trend removal for ensuring periodicity (Errico et al. 1985). Morever, Denis et al. (2002) have shown that there is no aliasing in the large scale.

We have also introduced an additional option to the original algorithm to assign each element of the variance array to two wavenumbers instead of one. Indeed, each element is located into a band delimited by two ellipses corresponding to two wavenumbers (k and k+1), the contribution to these two wavenumbers is distributed proportionally as a function of the distance to the two ellipses (see more details below). Moreover, an additional smoothing using a Bezier approximation can also applied when plotting the spectra.

It is worth noting that the same tool can be used to compute spectra for other models or observational data.

Contribution of each element of the variance array to two wavenumbers

Using the same formulation as Denis et al. (2002), the total variance can be expressed from spectral coefficients as:

$$\sigma^2 = \sum_{m=0}^{N_i-1} \sum_{n=0}^{N_j-1} \sigma^2(m,n),$$

with $(m,n) \neq (0,0)$, N_i and N_j the number of points for the two dimensions of the domain.

Analyzing data on rectangular domains conducts to use an elliptical truncation for constructing the power spectra. The normalisation of the m and n wavenumber axes by N_i and N_j leading to an elliptic shape. Thus, the normalized 2D wavenumber $\alpha(m,n)$ is defined as:

$$\alpha(m,n) = \sqrt{\frac{m^2}{N_i^2} + \frac{n^2}{N_j^2}}$$

An element in the variance array $\sigma^2(m,n)$ is located into a wavelength band between with $\alpha'(k) = \frac{k}{min(N_i,N_j)}$, k varying from 1 to min($N_i - 1$,$N_j - 1$).
Instead of adding the contribution $\sigma^2(m,n)$ only to wavenumber k as in Denis et al. (2002), an alternative way is to distribute this contribution between the two wavenumbers k and k+1 as follows:

- the contribution to $\sigma^2(\alpha'(k))$ is: $a_{m,n} * \sigma^2(m,n)$
- the contribution to $\sigma^2(\alpha'(k+1))$ is: $b_{m,n} * \sigma^2(m,n)$

with

$$\begin{cases} a_{m,n} = \frac{\alpha(m,n)-\alpha'(k)}{\alpha'(k+1)-\alpha'(k)} \\ b_{m,n} = \frac{\alpha'(k+1)-\alpha(m,n)}{\alpha'(k+1)-\alpha'(k)} \end{cases}$$

$a_{m,n}$ and $b_{m,n}$ representing weighting factors as a function of the distance to the limits $\alpha'(k)$ and $\alpha'(k+1)$.

2.6 GPS zenith delay

The Zenith Total Delay (ZTD) is obtained by vertically integrating the refractivity N:

$$ZTD \quad = \quad 10^{-6} \int_{z_r}^{\infty} k_1 \frac{P}{T_v} dz + 10^{-6} \int_{z_r}^{\infty} k_2^{'} \frac{e}{T} + k_3 \frac{e}{T^2} dz \tag{2.31}$$

where P, e are the total pressure and the partial pressure of water vapor, T_v is the virtual temperature, k_1, k_2 and k_3 are the atmospheric refractivity constants. The set proposed by Bevis et al. (1994) is used here: $k_1 = 77.60$ K hPa^{-1}, $k_2 = 69.4$ K hPa^{-1}, $k_3 = 370100$ K^2 hPa^{-1}.
The first term of (2.31) is called the zenith hydrostatic delay (ZHD), the second and third terms together are called the zenith wet delay (ZWD), which is proportional to the Integrated Water Vapor (IWV). More details can be found in Brenot et al. (2006).

2.7 Lidar products

This section is taken from Chaboureau et al. (2011). The lidar attenuated backscattered (ATB) signal corrected for geometric effects and calibration constant (expressed in m^{-1} sr^{-1}) at the altitude z and the wavelength λ is

$$\begin{aligned} ATB_\lambda(z) = & \quad [\beta_{mol,\lambda}(z) + \beta_{par,\lambda}(z)] \\ & \times \exp\left\{-2 \int_0^z \left[\alpha_{mol,\lambda}(z) + \eta\alpha_{par,\lambda}(z) dz\right]\right\} \end{aligned} \tag{2.32}$$

where α is the extinction coefficient (m^{-1}) and β the backscatter coefficient (m^{-1} sr^{-1}), both caused by air molecules (mol) and by aerosols and cloud particles (par). Multiple scattering by cloud particles is crudely taken into account with $\eta = 0.5$ (Platt 1973).

Following Collis and Russell (1976), the lidar backscatter and extinction coefficients for molecules, $\beta_{mol,\lambda}$ and $\alpha_{mol,\lambda}$ respectively, are

$$\beta_{mol,\lambda} = 5.45 \times 10^{-32} \times \frac{p}{k_B T} \times \left(\frac{\lambda}{0.55}\right)^{-4.09} \tag{2.33}$$

$$\alpha_{mol,\lambda} = \frac{8\pi}{3}\beta_{mol,\lambda} \tag{2.34}$$

where T is temperature (K), p is pressure (hPa), k_B is the Boltzmann constant (1.38×10^{-23} J K^{-1}), and wavelength λ is given in μm.

The optical properties of cloud particles and aerosols were integrated over their size distribution while extinction $Q_{ext,\lambda}$ and backscatter $Q_{back,\lambda}$ efficiencies were computed using the Mie code of **?** for spheres. Thus, particles were assumed to be spherical, although particle non-sphericity can be an important factor affecting the extinction to backscatter lidar ratio when the coarse mode prevails (Dubovik et al. 2006). Refraction indices of pure water and ice were used for cloud liquid and ice crystals respectively. In consistency with the numerical experiments, the refractive index of mineral dust was taken from Tulet et al. (2008), i.e., $1.448 - 2.92 \times 10^{-3}i$ at 532 nm, $1.44023 - 1.16 \times 10^{-3}i$ at 730 and 820 nm, and $1.41163 - 1.06 \times 10^{-3}i$ at 1064 nm.

For the 2-moment schemes, the integration over the size distribution of the particles $n_{par}(D, z)$ was performed using an accurate quadrature formula (here Gauss-Hermite for lognormal size distributions of dust) with

$$\alpha_{par,\lambda}(z) = \int_0^\infty \frac{\pi}{4} D^2 Q_{ext,\lambda}(D) n_{par}(D, z) dD \tag{2.35}$$

$$\beta_{par,\lambda}(z) = \int_0^\infty \frac{\pi}{4} D^2 Q_{back,\lambda}(D) n_{par}(D, z) dD \tag{2.36}$$

(The Gauss-Laguerre formula is used for γ-size distributions employed in the 2-moment microphysical schemes available in Meso-NH.) For the single-moment microphysical schemes, such as the one used here, $\alpha_{par,\lambda}$ and $\beta_{par,\lambda}$ were computed taking an effective radius representative of the distribution, in consistency with those employed for cloud and ice in the radiative scheme.

In each model column, the particle backscatter coefficient $\beta_{par,\lambda}$ and the extinction coefficient $\alpha_{par,\lambda}$ are both cloud particle and aerosol coefficients. They are computed from equations (2.35) and (2.36) using the model mixing ratios (and concentrations when available) of cloud particle and aerosol while the lidar backscatter and extinction coefficients for molecules are calculated using the model profiles of air density.

2.8 Radar products

Introduction

This section describes the computation of some standard radar products in the Meso-NH code using a generic representation of the hydrometeor size distributions.

The microphysical scheme assumes that each type of hydrometeor (rain, pristine ice, snow/aggregate, graupel, and hail) with an assigned index $i \in [r, i, s, g, h]$, follows a generalized gamma distribution, given below in the normalized form:

$$n_i(D)dD = N_i g_i(D)dD = N_i \frac{\alpha_i}{\Gamma(\nu_i)} \lambda_i^{\alpha_i \nu_i} D^{\alpha_i \nu_i - 1} \exp\{-(\lambda_i D)^{\alpha_i}\} dD \tag{2.37}$$

where D is the maximum dimension of the particules, N_i the concentration, ν_i and α_i, are dispersion parameters and λ_i the slope parameter. $\Gamma(x)$ is the gamma function (see Press et al. (1992) for the coding). The use of the generalized gamma law allows a greater flexibility in representing the particle size distribution while $M(p)$, the p^{th} moment of the law is easily computed as:

$$M_i(p) = \int_0^\infty D^p g_i(D)\, dD = \frac{G_i(p)}{\lambda_i^p}, \tag{2.38}$$

where

$$G_i(p) = \frac{\Gamma(\nu_i + p/\alpha_i)}{\Gamma(\nu_i)}. \tag{2.39}$$

With the notable exception of pristine ice (for which concentration is diagnosed), the one-moment microphysical scheme of Meso-NH assumes that N_i is a power function of λ_i (Caniaux et al. 1994):

$$N_i = C_i {\lambda_i}^{X_i}. \tag{2.40}$$

For example, taking $X_i = 0$ means that the total number concentration is held fixed while for $X_i = -1$, it is the intercept parameter ($N_0 \equiv C_i$) of a Marshall-Palmer distribution law (with $\nu_i = \alpha_i = 1$ in (2.37) to provide the classical form $n(D)dD = N_0\, e^{-\lambda D} dD$) which is kept constant. The model predicts mixing ratios, r_i which are expressed from (2.37) and the mass-diameter relationship ($m(D) = a_i D^{b_i}$):

$$\rho_{dref} r_i = \int_0^\infty m(D) n_i(D)\, dD = a_i N_i M_i(b_i) \tag{2.41}$$

where ρ_{dref} is the dry-air reference density of the anelatic system of equations. Using (2.40), (2.38) and (2.41), it is possible to compute the slope parameter λ_i as:

$$\lambda_i = \left(\frac{\rho_{dref} r_i}{a_i C_i G_i(b_i)}\right)^{\dfrac{1}{X_i - b_i}}. \tag{2.42}$$

2.8.1 Grid-point radar diagnostics

This subsection is partly reproduced in Richard et al. (2003). It is implicitly assumed that the radar wavelength is large enough so that radar waves propagate without attenuation and that the Rayleigh scattering approximation ($\propto D^6$ cross-section efficiency) is valid. Computations are made on the curvilinear "mass" grid system of the model.

Equivalent reflectivity factor: Z_e

The total equivalent radar reflectivity factor Z_e (dBZ), is calculated as a sum of radar reflectivities produced by each hydrometeor type which is illuminated by the radar wave (Ferrier 1994):

$$Z_e = 10\ \log_{10}\left[Z_{er} + Z_{ei} + Z_{es} + Z_{eg} + Z_{eh}\right]. \tag{2.43}$$

The rain contribution, Z_{er} has the simplest form

$$Z_{er} = 10^{18} \int_0^\infty n_r(D) D^6 dD \tag{2.44}$$

which is integrated using (2.38) and (2.39), to give:

$$Z_{er} = 10^{18} C_r G_r(6) \lambda_r{}^{x_r - 6}. \tag{2.45}$$

The case of ice particules is a little bit more difficult to treat because one must consider the melted diameter of the particles (D_e) and also the possible partial coating of these particles by a liquid film. The last effect is important because solid ice has a reduced specific dielectric factor of 0.224 which explains, for instance, the formation of a bright band when the snowflakes are falling accross the melting level.

For the snow/aggregate category, Z_{es} is thus given by

$$Z_{es} = 10^{18} \int_0^\infty 0.224 n_s(D_e) D_e^6 dD_e \tag{2.46}$$

with D_e deduced from

$$m_i(D) = a_i D^{b_i} = \frac{\pi}{6} \rho_w D_e^3 = m_r(D_e) \tag{2.47}$$

where ρ_w stands for liquid-water density, so inserting (2.47) into (2.46) with $n_s(D)\ dD = n_s(D_e)\ dD_e$ and performing the integration of (2.46) yields

$$Z_{es} = 0.224 \times 10^{18} \left(\frac{6}{\pi} \frac{a_s}{\rho_w} \right)^2 C_s G_s(2b_s) \lambda_s^{X_s - 2b_s}. \tag{2.48}$$

The snow category is composed of large ice crystals and of dry assemblages of smaller ice crystals. Only a small amount of light rime is allowed for these particles because they are converted into densely rimed graupels when much supercooled water is collected. Furthermore, the snowflakes are progressively converted into graupel-like hydrometeors when they go through the melting level. So it is assumed that the snow/aggregate category is exclusively composed of dry ice without unfrozen liquid water.

A similar assumption is made for pristine ice. As the concentration of ice N_i is diagnosed (therefore $\lambda_i = [(\rho_{dref}\, r_i)/(a_i N_i G_i(b_i))]^{-1/b_i}$), the equivalent radar reflectivity factor of the pristine ice, Z_{ei} is given by:

$$Z_{ei} = 0.224 \times 10^{18} \left(\frac{6}{\pi} \frac{a_i}{\rho_w} \right)^2 N_i G_i(2b_i) \lambda_i^{-2b_i}. \tag{2.49}$$

The equivalent radar reflectivity factor of the graupel, Z_{eg} is given by

$$Z_{eg} = \begin{cases} 10^{18} \int_0^\infty \{0.224(1 - f_c(D_e)) + f_c(D_e)\} n_g(D_e) D_e^6 dD_e & \text{for } T < 273.16 \text{ K}, \\ 10^{18} \int_0^\infty n_g(D_e) D_e^6 dD_e & \text{for } T > 273.16 \text{ K}, \end{cases} \tag{2.50}$$

with again D_e defined by (2.47). The water coating factor f_c has been set to an empirical constant value of 0.14 as suggested by Rasmussen et al. (1984). The same was done by Walko et al. (1995) to compute the shedding rate of the hailstones. It is assumed also that the graupel are fully wetted hydrometeors below the melting level ($T > 273.16$ K). Integration of (2.50) leads to

$$Z_{eg} = \begin{cases} 0.333 \times 10^{18} \left(\frac{6}{\pi} \frac{a_g}{\rho_w} \right)^2 C_g G_g(2b_g) \lambda_g^{X_g - 2b_g} & \text{for } T < 273.16 \text{ K}, \\ 10^{18} \left(\frac{6}{\pi} \frac{a_g}{\rho_w} \right)^2 C_g G_g(2b_g) \lambda_g^{X_g - 2b_g} & \text{for } T > 273.16 \text{ K}. \end{cases} \tag{2.51}$$

The equivalent reflectivity of hail Z_{eh} is simply given by:

$$Z_{eh} = 10^{18}\Big(\frac{6}{\pi}\frac{a_h}{\rho_w}\Big)^2 C_h G_h(2b_h)\lambda_h^{X_h-2b_h} \tag{2.52}$$

because it is assumed that the hailstones are fully coated by a liquid film as a result of the ”wet mode” growth of these particles with a continuous water shedding.

Equivalent Doppler velocity: V_{Dop}

The equivalent Doppler velocity is computed for a vertically pointing radar located at the base of each column of the model grid system. The general formula is the following:

$$V_{Dop} = \frac{\displaystyle\sum_{i\in[r,s,g,h]} \int_0^\infty z_i(D) v_i(D) dD}{\displaystyle\sum_{i\in[r,s,g,h]} \int_0^\infty z_i(D) dD} \tag{2.53}$$

where $z_i(D)\ dD = n_i(D)D^6\ dD$ (or $z_i(D_e)\ dD_e = 0.333 * n_i(D_e)D_e^6\ dD_e$ in the more general case of partially wetted ice particles) is the intrinsic reflectivity of an hydrometeor of type ”i”. The fall speed is given by $v_i(D) = c_i D^{d_i}(\rho/\rho_{00})^{0.4}$ with air density ρ effect (Foote and Du Toit 1969) (ρ_{00} corresponds to the ground level) so making the integration of (2.53) straightforward.

Differential reflectivity: Z_{DR}

The differential reflectivity is only computed for the raindrops, a major contribution of the polarimetric signal, according the following definition of Z_{DR}

$$Z_{DR} = 10\ \log_{10}\left[\frac{\displaystyle\int_0^\infty z_r^{HH}(D)dD}{\displaystyle\int_0^\infty z_r^{VV}(D)dD}\right] \tag{2.54}$$

where z_r^{HH} is the intrinsic reflectivity of a H-polarized wave received on a H-polarized antenna and the same for z_r^{VV} but for the V orthogonal direction. The differential signal is due to the deformation of the raindrops as their size increases thus $z_r^{HH} > z_r^{VV}$ because big raindrops get an oblate shape. The mean axis ratio, $r(D)$, is generally given with a polynomial expansion of the form (Chuang and Beard 1990):

$$r(D) = \sum_j r_j D^j. \tag{2.55}$$

A widely used representation of $r(D)$ is the equilibrium axis ratio model given by Pruppacher and Beard (1970):

$$r(D) = 1.03 - 0.62 \times 10^2 \times D \tag{2.56}$$

but as stressed by Jameson (1983), multiple modes of drop oscillations make the computations even more difficult. The more recent study of Andsager et al. (2016) takes into account this effect and recommands a quadratic polynomial fitting.

$$r(D) = 1.012 - 0.144 \times 10^2 \times D - 1.03 \times 10^4 \times D^2. \tag{2.57}$$

With the approximation $z_r^{HH}(D) \sim r(D)^{-7/3} \times z_r^{VV}(D)$ (Jameson 1983) and taking $z_r^{VV}(D) = n_r(D)\ D^6$, an analytical expression for (2.54) can be derived using (2.57) and expanding $r(D)^{1/3}$ up to the second order:

$$Z_{DR} = -10\ \log_{10}\Bigg[1.012^{7/3}(1 - \left(\tfrac{7}{3}\right)\left(\tfrac{0.144\times10^2}{1.012}\right)\tfrac{G(7)}{G(6)}\tfrac{1}{\lambda_r} + \left[-\left(\tfrac{7}{3}\right)\left(\tfrac{1.03\times10^4}{1.012}\right) + \left(\tfrac{14}{9}\right)\left(\tfrac{0.144\times10^2}{1.012}\right)^2\right]\tfrac{G(8)}{G(6)}\tfrac{1}{\lambda_r^2} + \cdots)\Bigg] \tag{2.58}$$

giving

$$Z_{DR} = -10\ \log_{10}\left[1.0282 \times \left(1 - 33.20\frac{G(7)}{G(6)}\frac{1}{\lambda_r} - 23433.4\frac{G(8)}{G(6)}\frac{1}{\lambda_r^2}\right)\right]. \tag{2.59}$$

We recall that a complete calculation of Z_{DR} would need to take into account the contribution of the ice particles for which the "mean" shape asymmetry in a turbulent motion is not well known. Since ice particles tend to scatter energy like spheres, the Z_{DR} for snow and hail will be near zero but, negative Z_{DR} may occur for conically-shaped graupel.

Specific differential phase: K_{DP}

The specific differential phase K_{DP} is obtained from

$$K_{DP} = \frac{180\lambda}{\pi}\int_0^\infty Re\{f_H(D) - f_V(D)\}n(D)dD \tag{2.60}$$

where $f_H(D) - f_V(D)$ are the forward scatter amplitudes at H- and V-polarization. From (2.60), Jameson (1985) derived a relation between specific differential phase and the water content and raindrop axis ratio. For a C and S-band radar wave with centimetric λ (~ 0.1 m), K_{DP} is approximated by

$$K_{DP} = 10^3 \times \frac{180\lambda}{\pi}C\int_0^\infty D^3(1 - r(D))n(D)dD. \tag{2.61}$$

The 10^3 factor means that K_{DP} is in the conventional deg km^{-1} unit. Values of C depend on the radar frequency; $C = 0.05717 \times 10^4$ at $\lambda = 0.1071$ m and $C = 0.5987 \times 10^4$ at $\lambda = 0.0321$ m. After rearrangement of (2.61), one obtains:

$$K_{DP} = 10^3 \times \frac{180\lambda}{\pi}\frac{6C}{\pi\rho_w}(\rho_a r_r)\left[1.0 - \int_0^\infty D^3 r(D)n(D)dD\Big/\int_0^\infty D^3 n(D)dD\right] \tag{2.62}$$

At $\lambda = 10.71$ cm and using (2.57), one finally gets:

$$K_{DP} = 6.7\ 10^3 \times (\rho_a r_r)\left[0.144 \times 10^2\frac{G(4)}{G(3)}\frac{1}{\lambda_r} + 1.03 \times 10^4\frac{G(5)}{G(3)}\frac{1}{\lambda_r^2}\right]. \tag{2.63}$$

In the above expression, K_{DP} is forced to zero in the absence of rain. Note that with the equivalent C value at $\lambda = 10.71$ cm suggested by Gorgucci et al. (2002) one gets 6.3 instead of 6.7 in (2.63).

2.8.2 Radar diagnostics on Plan Position Indicators (PPI)

An alternative simulator simulates Plan Position Indicators (PPI), which are cones usually projected on a horizontal plane obtained by scanning the atmosphere at constant elevation. This simulator is meant to allow for direct comparisons with conventional radar outputs[1]. The main differences with the grid-point simulator are:

- possibility to choose among several scattering models,
- beam bending taken into account,
- possibility to take attenuation into account,
- antenna's radiation pattern (beam broadening) modeled,
- ouptut on Cartesian grids (compatible with the operational French radar products).

This subsection explains all these differences.

Radar equation

Here, the assumptions made for the grid-point simulator are relaxed. So we have to use the radar equation to express radar observations, and equivalent radar reflectivity factor in particular. The radar equation relates the power P_t (in W) emitted by the radar to the received one (P_r, in W). It can be written without much loss of generality as (see, e.g., Doviak and Zrnić 1993):

$$\overline{P_r}(\boldsymbol{r}_0) = \frac{P_t g^2 \lambda^2}{(4\pi)^3} \int_0^{\infty} \int_0^{2\pi} \int_0^{\pi} \frac{\eta(\boldsymbol{r}) l(\boldsymbol{r})^2}{r^4} f^4(\vartheta', \phi') |W(r_0 - r)|^2 r^2 \sin\vartheta' dr d\vartheta' d\phi' \,, \tag{2.64}$$

where

- $\boldsymbol{r}_0$ (in m) is the vector that links the radar emitting antenna to the centre of the resolution volume,
- g is the gain in emission of the antenna, which normally includes attenuation by radome and waveguide,
- λ (in m) is the wavelength of the emitted signal,
- $\boldsymbol{r}$ (in m), with spherical coordinates (r, ϑ, ϕ) (see Fig. 2.1), is the vector that links the antenna to the current point,
- f^2 is the angular weighting function,
- W is the radial weighting function,
- η (in m^{-1}) is the *radar reflectivity*, which is defined by

  $$\eta(\boldsymbol{r}) \equiv \frac{1}{\delta\mathcal{V}} \sum_{i\in\delta\mathcal{V}} \sigma_i = \sum_{j\in\text{type}} \int_0^{\infty} \sigma_j(D) N_j(D, \boldsymbol{r}) dD \,, \tag{2.65}$$

  where σ_i (in m^2) is the *backscattering cross-section* of the i^{th} scatterer located in the infinitesimal volume $\delta\mathcal{V}$ (in m^3), $\sigma_j(D)$ (in m^2) is the backscattering section of particles of diameter D (in m) with respect to their types j (precipitating water, graupel, snow, primary ice[2]), and N_j (in m^{-4}) is the hydrometeor size distribution.

---

[1] Note that it is not yet possible to simulate Range Height Indicator (RHI), which is obtained by scanning in the vertical at a constant azimuth.

[2] Hail is not yet included in the current version. Note, however, that the effect of primary ice is taken into account.

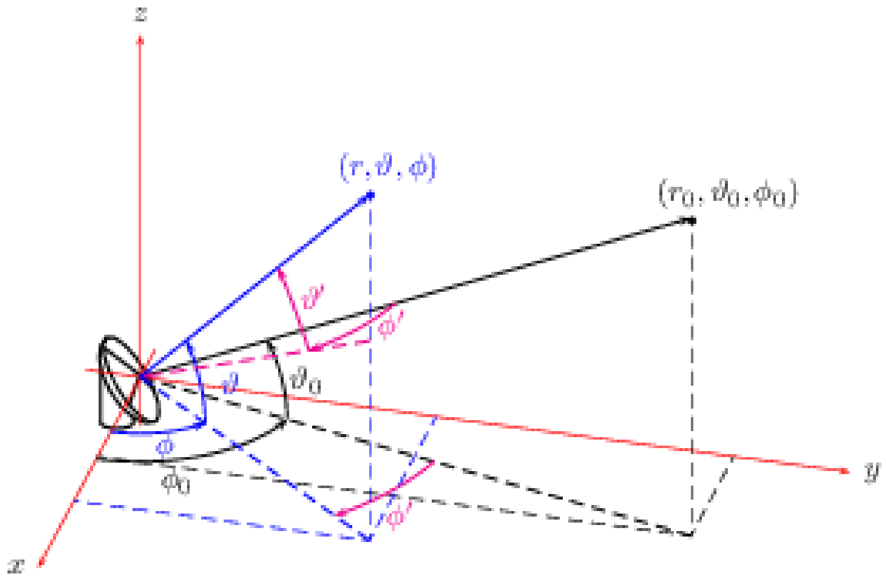

Figure 2.1: Spherical coordinates used to locate the target.

- l is the total attenuation:

$$l(\boldsymbol{r}) = \exp\left(-\int_0^r \sum_{j\in\text{type}} \int_0^\infty C_{ej}(D)N_j(D,\boldsymbol{r})dDdr\right) , \tag{2.66}$$

  where C_{ej} is the *extinction cross-section* of the j^{th} scatterer.

When

1. the resolution volume is small enough so that hydrometeor properties are uniform inside this volume,
2. the Rayleigh approximation is valid (wavelength much smaller than particle sizes),
3. scatterers are only made of liquid water,
4. attenuation is negligible,
5. the receiver's bandwidth is infinite,
6. the antenna's directivity function is Gaussian,

then (2.64) can be written as

$$P_r(\boldsymbol{r}_0) = C\frac{z(\boldsymbol{r}_0)}{r_0^2} , \tag{2.67}$$

where

$$z \equiv \int_0^\infty D^6 N_r(D)dD , \tag{2.68}$$

is the *radar reflectivity factor* and

$$C \equiv \frac{\pi^3 P_t g^2 c\tau(\Delta\vartheta)^2|K_w|^2}{1024\lambda^2 \ln 2} \tag{2.69}$$

is the *radar constant*, where c is the celerity of light in vacuum ($\mathrm{m\ s^{-1}}$), τ is the pulse duration (s), $\Delta\vartheta$ is the beam width to the -3 dB level for one-way transmission (rad), $|K_w|^2$ is the *dielectric factor* for water (about 0.93 for usual wavelengths). Under these assumptions, note that (2.68) and (2.44) are strictly identical (except that the units differ).

When the previous assumptions are not met, the radar measures *equivalent reflectivity factors* which can be simulated by:

$$\bar{z}_e(\boldsymbol{r}_0) \equiv \frac{r_0^2 P_r(\boldsymbol{r}_0)}{C} = \frac{16 r_0^2 \lambda^4 \ln 2}{\pi^6 c\tau (\Delta\vartheta)^2 |K_w|^2} \int_0^{2\pi}\int_0^{\pi}\int_0^{\infty} \frac{\eta(\boldsymbol{r}) l(\boldsymbol{r})^2}{r^2} f^4(\vartheta', \phi') |W(r_0 - r)|^2 \sin\vartheta' dr d\vartheta' d\phi' . \tag{2.70}$$

Since the equivalent reflectivity factor takes values within several orders of magnitude, it is commonly expressed in dBZ:

$$\bar{Z}_e \equiv 10 \log\left(10^{18} \bar{z}_e\right) . \tag{2.71}$$

At present, the radar simulator does not take into account the finite bandwidth effect. So the expression used to compute reflectivities reads:

$$\bar{z}_e(\boldsymbol{r}_0) = \frac{8\lambda^4 \ln 2}{\pi^6 (\Delta\vartheta)^2 |K_w|^2} \int_0^{2\pi}\int_0^{\pi} \eta(\boldsymbol{r}) l(\boldsymbol{r})^2 f^4(\vartheta', \phi') \sin\vartheta' d\vartheta' d\phi' . \tag{2.72}$$

The article by Caumont et al. (2006) summarizes this paragraph and provides an example of use of the reflectivity simulator on a case study.

With the same formalism as for reflectivity, Doppler velocity is expressed as follows:

$$v_r(\boldsymbol{r}_0) = \frac{\displaystyle\int_0^{2\pi}\int_0^{\pi} \overline{\eta v_r}(\boldsymbol{r}) l(\boldsymbol{r})^2 f^4(\vartheta', \phi') \sin\vartheta' d\vartheta' d\phi'}{\displaystyle\int_0^{2\pi}\int_0^{\pi} \eta(\boldsymbol{r}) l(\boldsymbol{r})^2 f^4(\vartheta', \phi') \sin\vartheta' d\vartheta' d\phi'} , \tag{2.73}$$

with

$$\overline{\eta v_r}(\boldsymbol{r}) \equiv \sum_{j \in \text{type}} \int_0^{\infty} \sigma_j(D, \boldsymbol{r}) \left(u_r(\boldsymbol{r}) - \sin\vartheta v_{T_j}(D, \boldsymbol{r})\right) N_j(D, \boldsymbol{r}) dD , \tag{2.74}$$

$$= \eta(\boldsymbol{r}) u_r(\boldsymbol{r}) - \sin\vartheta \sum_{j \in \text{type}} \int_0^{\infty} \sigma_j(D, \boldsymbol{r}) v_{T_j}(D, \boldsymbol{r}) N_j(D, \boldsymbol{r}) dD , \tag{2.75}$$

where $u_r(\boldsymbol{r})$ is the projection onto the beam direction of the wind vector (in m s^{-1}), and $v_{T_j}(D, \boldsymbol{r})$ is the fall speed of particles of diameter D (in m) for the precipitating hydrometeor type j (in m s^{-1}). More details about the simulation of Doppler velocities are provided by Caumont and Ducrocq (2008).

A similar, yet more general expression than in the grid-point simulator (cf. (2.54)), is used to compute differential reflectivity (in dB) (see Seliga and Bringi 1976):

$$Z_{DR} \equiv 10 \log \frac{z_{HH}}{z_{VV}} \tag{2.76}$$

where z_{HH} and z_{VV} are equivalent reflectivity factors (in $\mathrm{mm^6\ m^{-3}}$) at horizontal and vertical polarization, respectively.

Specific differential phase is computed from (2.60) with a factor of 10^3 to express it in $^\circ\ \mathrm{km^{-1}}$.

Note that, as in the grid-point simulator, only raindrops contribute to Z_{DR} and K_{DP}. Raindrops are considered as spheroids (when the scattering model allows for it; see below), the axis ratios of which are defined by (2.56) or (2.57), as in the grid-point simulator.

Numerical implementations

Integrals over D. (2.65), (2.66), (2.72), and (2.73) contain improper integrals that cannot be directly computed. The angular double quadratures in (2.72) and (2.73) are evaluated by following the method of Probert-Jones (1962), i.e., considering the antenna's radiation pattern as a Gaussian function, which means that only the main lobe is taken into account. Two similar techniques are implemented: Gauss-Hermite's and Gauss-Legendre's. In the following, $\eta(\boldsymbol{r})l^2(\boldsymbol{r})$ or $\overline{\eta v_r}(\boldsymbol{r})l(\boldsymbol{r})^2$ are denoted as $F(\boldsymbol{r})$.

Gauss-Hermite quadrature. The first technique consists in approaching the bidimensional integral by two independent integrals over $]-\infty;\infty[$:

$$I = \int_0^{2\pi}\int_0^{\pi} f^4(\vartheta',\phi')F(\boldsymbol{r})\sin\vartheta' d\vartheta' d\phi' = \int_{-\infty}^{\infty}\int_{-\infty}^{\infty} e^{-8\ln 2\frac{\vartheta'^2}{\Delta\vartheta^2}} e^{-8\ln 2\frac{\phi'^2}{\Delta\vartheta^2}} F(\boldsymbol{r}) d\vartheta' d\phi' \,. \tag{2.77}$$

Then, the so-called Gauss-Hermite quadrature is used to evaluate the two improper integrals:

$$I \underset{\binom{x}{y}=\frac{\sqrt{8\ln 2}}{\Delta\vartheta}\binom{\vartheta'}{\phi'}}{=} \frac{(\Delta\vartheta)^2}{8\ln 2}\int_{-\infty}^{\infty} e^{-x^2}\int_{-\infty}^{\infty} e^{-y^2} F\left(r,\vartheta_0+\frac{x\Delta\vartheta}{\sqrt{8\ln 2}},\phi_0+\frac{y\Delta\vartheta}{\sqrt{8\ln 2}}\right) dydx \,, \tag{2.78}$$

$$\simeq \frac{(\Delta\vartheta)^2}{8\ln 2}\sum_{i=0}^{n_H-1}\sum_{j=0}^{n_V-1} v_i w_j F\left(r,\vartheta_0+\frac{x_i\Delta\vartheta}{\sqrt{8\ln 2}},\phi_0+\frac{y_j\Delta\vartheta}{\sqrt{8\ln 2}}\right) \,, \tag{2.79}$$

where x_i and y_i are abscissas for the quadrature, v_i and w_i are the corresponding weights, and n_H and n_V are the corresponding numbers of abscissas.

Gauss-Legendre quadrature. The second technique consists in approaching the bidimensional integral by two independent integrals over $]-\Delta\vartheta/2;\Delta\vartheta/2[$:

$$I \simeq \int_{-\Delta\vartheta/2}^{\Delta\vartheta/2}\int_{-\Delta\vartheta/2}^{\Delta\vartheta/2} e^{-8\ln 2\frac{\vartheta'^2}{\Delta\vartheta^2}} e^{-8\ln 2\frac{\phi'^2}{\Delta\vartheta^2}} F(\boldsymbol{r}) d\vartheta' d\phi' \,, \tag{2.80}$$

$$\underset{\binom{x}{y}=\frac{\Delta\theta}{2}\binom{\vartheta'}{\phi'}}{\simeq} \frac{(\Delta\theta)^2}{4}\int_{-1}^{1} e^{-2\ln 2x^2}\int_{-1}^{1} e^{-2\ln 2y^2} F\left(r,\theta_0+\frac{x\Delta\theta}{2},\phi_0+\frac{y\Delta\theta}{2}\right) dydx \,, \tag{2.81}$$

$$\simeq \frac{(\Delta\theta)^2}{4}\sum_{i=0}^{n_H-1}\sum_{j=0}^{n_V-1} v_i w_j e^{-2\ln 2x_i^2} e^{-2\ln 2y_j^2} F\left(r,\vartheta_0+\frac{x_i\Delta\vartheta}{2},\phi_0+\frac{y_j\Delta\vartheta}{2}\right) \,, \tag{2.82}$$

where x_i, y_i, v_i, w_i, n_H, and n_V have similar roles as in the Gauss-Hermite quadrature, but correspond here to the Gauss-Legendre one.

The Gauss-Hermite quadrature is well-suited for low numbers of points (typically ≤ 3), whereas the Gauss-Legendre quadrature is better suited for high number of points: above 3 points, the Gauss-Hermite quadrature evaluates the function in the integral for angles that are unrealistically far away from the direction of propagation, while under 3 points, the Gauss-Legendre quadrature does not provide consistent values, i.e., for $n_H = n_V = 1$:

$$\frac{(\Delta\theta)^2}{4} v_0 w_0 e^{-2\ln 2x_0^2} e^{-2\ln 2y_0^2} F\left(r_0,\theta_0,\phi_0\right) = (\Delta\theta)^2 F\left(\boldsymbol{r}_0\right) \tag{2.83}$$

which is different from $\frac{\pi(\Delta\theta)^2}{8\ln 2}F\left(\boldsymbol{r}_0\right) \simeq 0.567(\Delta\theta)^2F\left(\boldsymbol{r}_0\right)$ as would give a simple evaluation at the centre of the volume of resolution.

Similarly, the improper integral involving scatterer diameters is computed by using a Gauss-Laguerre quadrature. Further details concerning these quadrature techniques can be found in Press et al. (1992).

Scattering methods. Four methods are available: Rayleigh (for spheres), Mie, Rayleigh for spheroids and T-Matrix.

Rayleigh, Mie or Rayleigh for spheroids scattering methods

The three first methods have been implemented and are described by Caumont et al. (2006). When using Rayleigh, Mie or Rayleigh for spheroids methods, hydrometeors containing ice are supposed to behave as isotropic scatterers as they fall or tumble (i.e., they are modeled as spheres). The approximations of Rayleigh for spheres and for spheroids yield analytic results. Thus, for instance, in the Rayleigh theory, cross sections for raindrops are

$$\sigma_{\mathrm{HH}} = \frac{\pi^5|K_w^2|}{\lambda^4}D^6\,, \tag{2.84}$$

$$C_e = \frac{\pi^2}{\lambda}\Im K_w D^3 + \frac{\pi^4}{15\lambda^3}\Im\left(K_w^2\frac{m^4+27m^2+38}{2m^2+3}\right)D^5 + \frac{2\pi^5}{3\lambda^4}\Re(K_w^2)D^6\,. \tag{2.85}$$

Analytic derivations of Rayleigh for spheroids cross sections can be found in Kerker (1969) (Chap. 10), van de Hulst (1981), Doviak and Zrnić (1993), or Bringi and Chandrasekar (2001), for instance. Mie computations rely on the code described by Bohren and Huffman (1983).

For pure water particles, the dielectric function is taken from Liebe et al. (1991), while the model of Hufford (1991) is taken for pure ice. Here we make the following assumptions: for particles made of ice and air only (snow, primary ice, and graupel above the melting level), we consider the diameter of a sphere made of ice only that would have the same mass (e.g., Smith 1984). For water-coated graupel, which are made of ice, water, and air, we consider the diameter of an equivalent-mass sphere made of 14 % of water and 86 % of ice as spheroidal inclusions (following Rasmussen et al. 1984). The corresponding dielectric function is then computed following Bohren and Battan (1982).

T-matrix scattering method

When using T-matrix scattering method, implemented and described by Augros et al. (2016), not only raindrops but also snow and graupel particles are considered as spheroids. The T-matrix code has been adapted from Mishchenko and Travis (1998) and Mishchenko et al. (2002). T-matrix lookup tables containing the scattering coefficients were computed in advance for each hydrometeor type and each radar wavelength (S, C and X band). These coefficients were estimated for a set of diameters, temperatures, elevation angles and liquid water fractions for melting graupel. Polarimetric variables are calculated from the scattering coefficients following the equations given in the Appendix of Augros et al. (2016).

When selecting T-matrix scattering method, a more continuous melting process is simulated for graupel particles. In a similar way to Jung et al (2008), the water fraction inside graupel particles is estimated as a function of the hydrometeor contents of graupel and rain M_g and M_r. More details of this parameterization are explained by Augros et al. (2016).

2.9 Satellite diagnostics

A comparison between model outputs and satellite observations provides an assessment of how well the model can reproduce the meteorological situation. The model-to-satellite approach compares directly the satellite brightness temperatures (BTs) to the BTs computed from the predicted model fields (Morcrette 1991). It has been first applied to Meso-NH outputs for comparison with Meteosat observations in the infrared using a narrow-band code (Chaboureau et al. 2000), then for the tuning of a critical parameter in the microphysical scheme (Chaboureau et al. 2002).

Since the Masdev 4-7 version, the Radiative Transfer for Tiros Operational Vertical Sounder (RTTOV) code version 11.3 (Saunders et al. 2005) is also available allowing the calculation of BT for a large number of satellites. RTTOV was first used with Meso-NH for a further tuning in the microphysical scheme (Chaboureau and Pinty 2006). The paragraphs below are taken from the RTTOV documentation. They give a broad overview on the RTTOV model. More information can be obtained from the web ressources on `https://nwpsaf.eu/site/software/rttov/`

The RTTOV model allows rapid simulations of radiances for satellite infrared or microwave nadir scanning radiometers given an atmospheric profile of temperature, variable gas concentrations, cloud and surface properties. Ozone and carbon dioxide are taken from the McClatchey et al. (1972) standard profiles and the fixed value used in Meso-NH, respectively. Above the model top, the standard profiles from McClatchey et al. (1972) are used. All the atmospheric profiles of temperature and gas concentrations are then interpolated onto the 43 pressure levels of RTTOV.

Currently the spectral range of the RTTOV model is 3-20 μm (500-3000 cm^{-1}) in the infrared governed by the range of the GENLN2 line-by-line dataset on which it is based. In the microwave the frequency range from 10-200 GHz is covered using the Liebe-89 MPM line-by-line model. The full list of currently supported platforms and sensors is given in Tables 2 and 3 of the RTTOV users guide (and duplicated on the Meso-NH users guide). Simulation of clear radiances are based on transmittances computed by means of a linear regression in optical depth.

In the infrared, the RTTOV code takes clouds into account as grey bodies (Chevallier et al. 2001) on the Meso-NH defined model level assuming maximum random overlap of clouds. Radiative properties for water clouds are calculated using constants tabulated in Hu and Stamnes (1993). Water cloud effective radius is diagnosed using a value of 10 μm over land and 13 μm over sea. Radiative properties for ice clouds are taken from Baran and Francis (2004) assuming hexagonal columns with an effective dimension diagnosed from the ice water content (McFarquhar et al. 2003). Surface emissivity is given by the Ecoclimap database (Masson et al. 2003). Note that the surface emissivity is valid there for a broad band between 8 and 12 μm only.

In the microwaves, the hydrometeor optical properties are provided to the RTTOV model from precomputed Mie tables for liquid water, cloud ice, rain, and precipitating ice (Bauer 2001). The cloud layers are overlapped following a maximum random approximation. Polarization is only introduced by the sea surface properties obtained using the FASTEM code. Elsewhere (over land and sea-ice) surface emissivity is fixed with typical value of bare soil.

2.10 References

Ahmed, N. N. and K. R. Rao, 1974: Discrete cosine transform. *IEEE Trans. Comput.*, **C-23**, 90–93.

Andsager, K., K. V. Beard, and N. F. Laird, 2016: Laboratory measurements of axis ratios for large raindrops. *J. Atmos. Sci.*, **56**, 2673–2683.

Augros, C., V. Caumont, O. Ducrocq, N. Gaussiat, and P. P. Tabary, 2016: Comparisons between S, C, and X band polarimetric radar observations and convective-scale simulations of HyMeX first special observing period. *Quart. J. Roy. Meteor. Soc.*, **142**, 347–362, doi:10.1002/qj.2572.

Baran, A. J. and P. N. Francis, 2004: On the radiative properties of cirrus cloud at solar and thermal wavelengths: a test of model consistency using high-resolution airbone radiance measurements. *Quart. J. Roy. Meteor. Soc.*, **130**, 763–778, doi:10.1256/qj.03.151.

Bauer, P., 2001: Including a melting layer in microwave radiative transfer simulations for clouds. *Atmos. Res.*, **57**, 1619–1632.

Bevis, M., S. Businger, S. Chiswell, T. Herring, R. A. Anthes, C. Rocken, and R. H. Ware, 1994: GPS meteorology: Mapping zenith wet delays onto precipitable water. *J. Appl. Meteorol.*, **33**, 379–386.

Bohren, C. F. and L. J. Battan, 1982: Radar backscattering of microwaves by spongy ice spheres. *J. Atmos. Sci.*, **39**, 2623–2628.

Bohren, C. F. and D. R. Huffman, 1983: *Absorption and scattering of light by small particles*. John Wiley and Sons.

Bolton, D., 1980: The computation of equivalent potential temperature. *Mon. Weather Rev.*, **108**, 1046–1053.

Brasseur, O., 2001: Development and application of a physical approach to estimating wind gusts. *Mon. Weather Rev.*, **129**, 5–25, doi:10.1175/1520-0493(2001)129⟨0005:DAAOAP⟩2.0.CO;2.

Brenot, H., V. Ducrocq, A. Walpersdorf, C. Champollion, and O. Caumont, 2006: GPS zenith delay sensitivity evaluated from high-resolution numerical weather prediction simulations of the 8-9th September 2002 flash flood over southeastern France. *J. Geophys. Res.*, **111**, doi: 10.1029/2004JD005726.

Bringi, V. N. and V. Chandrasekar, 2001: *Polarimetric Doppler weather radar: Principles and applications*. Cambridge University Press, 636 pp.

Caniaux, G., J.-L. Redelsperger, and J.-P. Lafore, 1994: A numerical study of the stratiform region of a fast-moving squall line. Part I: General description and water and heat budgets. *J. Atmos. Sci.*, **13**, 2046–2074.

Caumont, O. and V. Ducrocq, 2008: What should be considered when simulating doppler velocities measured by ground-based weather radars? *J. Appl. Meteorol. Clim.*, **47**, 2256–2262, doi:10.1175/2008JAMC1894.1.

Caumont, O., et al., 2006: A radar simulator for high-resolution nonhydrostatic models. *J. Atmos. Ocean. Tech.*, **23**, 1049–1067, doi:10.1175/JTECH1905.1.

Chaboureau, J.-P., J.-P. Cammas, P. Mascart, J.-P. Pinty, C. Claud, R. Roca, and J.-J. Morcrette, 2000: Evaluation of a cloud system life-cycle simulated by the Meso-NH model during FASTEX using METEOSAT radiances and TOVS-3I cloud retrievals. *Quart. J. Roy. Meteor. Soc.*, **126**, 1735–1750, doi:10.1002/qj.49712656609.

Chaboureau, J.-P., J.-P. Cammas, P. J. Mascart, J.-P. Pinty, and J.-P. Lafore, 2002: Mesoscale model cloud scheme assessment using satellite observations. *J. Geophys. Res.*, **107**, 4301, doi: 10.1029/2001JD000714.

Chaboureau, J.-P. and J.-P. Pinty, 2006: Validation of a cirrus parameterization with Meteosat Second Generation observations. *Geophys. Res. Lett.*, **33**, L03 815, doi:10.1029/2005GL024725.

Chaboureau, J.-P., et al., 2011: Long-range transport of Saharan dust and its radiative impact on precipitation forecast over western Europe: a case study during the Convective and Orographically induced Precipitation Study (COPS). *Quart. J. Roy. Meteor. Soc.*, **137**, 236–251, doi:10.1002/qj.719.

Chaboureau, J.-P., et al., 2016: Fennec dust forecast intercomparison over the Sahara in June 2011. *Atmos. Chem. Phys.*, **16**, 6977–6995, doi:10.5194/acp-16-6977-2016.

Chevallier, F., P. Bauer, G. Kelly, C. Jakob, and T. McNally, 2001: Model clouds over oceans as seen from space: comparison with HIRS/2 and MSU radiances. *J. Climate*, **14**, 4216–4229, doi:10.1175/1520-0442(2001)014%3C4216:MCOOAS%3E2.0.CO;2.

Chuang, C. and K. V. Beard, 1990: A numerical model for the equilibrium shape of electrified raindrops. *J. Atmos. Sci.*, **47**, 1374–1389.

Collis, R. T. and P. B. Russell, 1976: *Laser monitoring of the atmosphere*. Springer-Verlag.

Couvreux, F., F. Hourdin, and C. Rio, 2010: Resolved versus parametrized boundary-layer plumes. Part I: a parametrization-oriented conditional sampling in large-eddy simulations. *Bound.-Layer. Meteor.*, **134**, 441–458, doi:10.1007/s10546-009-9456-5.

Dauhut, T., J.-P. Chaboureau, J. Escobar, and P. Mascart, 2016: Giga-LES of Hector the Convector and its two tallest updrafts up to the stratosphere. *J. Atmos. Sci.*, **73**, 5041–5060, doi:10.1175/JAS-D-16-0083.1.

Denis, B., J. Côté, and R. Laprise, 2002: Spectral decomposition of two-dimensional atmospheric fields on limited-area domains using the discrete cosine transform (DCT). *Mon. Weather Rev.*, **130**, 1812–1829.

Doviak, R. J. and D. S. Zrnić, 1993: *Doppler Radar and Weather Observations*. 2nd Ed. Academic Press, Cambridge University Press, 562 pp.

Dubovik, O., et al., 2006: Application of spheroid models to account for aerosol particle nonsphericity in remote sensing of desert dust. *J. Geophys. Res.*, **111 (D11208)**, doi:10.1029/2005JD006619.

Emanuel, K. A., 1994: *Atmospheric convection*. Oxford University Press.

Ferrier, B. S., 1994: A double-moment multiple-phase four-class bulk ice scheme. Part I: Description. *J. Atmos. Sci.*, **51**, 249–280.

Foote, G. B. and P. S. Du Toit, 1969: Terminal velocity of raindrops aloft. *J. Appl. Meteorol.*, **8**, 249–253.

Gorgucci, E., V. Chandrasekar, V. N. Bringi, and G. Scarchilli, 2002: Estimation of raindrop size distribution parameters from polarimetric radar measurements. *J. Atmos. Sci.*, **59**, 2373–2384.

Hill, R. J., S. F. Clifford, and R. S. Lawrence, 1980: Refractive index and absorption fluctuations in the infrared caused by temperature, humidity, and pressure-fluctuations. *J. Opt. Soc. Am.*, **70**, 1192–1205.

Hu, Y. X. and K. Stamnes, 1993: An accurate parameterization of the radiative properties of water clouds suitable for use in climate models. *J. Climate*, **6**, 728–742.

Hufford, G., 1991: A model for the complex permittivity of ice at frequencies below 1 THz. *Intnl. J. Infrared and Millimetre Waves*, **12**, 677–681.

Jameson, A. R., 1983: Microphysical interpretation of multi-parameter radar measurements in rain. Part I: Interpretation of polarization measurements and estimation of raindrop shapes. *J. Atmos. Sci.*, **40**, 1792–1802.

Jameson, A. R., 1985: Microphysical interpretation of multi-parameter radar measurements in rain. Part III: Interpretation and measurement of propagation differential phase shift between orthogonal linear polarizations. *J. Atmos. Sci.*, **42**, 607–614.

Kerker, M., 1969: *The Scattering of Light and other Electromagnetic Radiation*. Academic Press, Inc., New York, New York, 666 pp.

Koshyk, J. N., K. Hamilton, and J. D. J. D. Mahlman, 1999: Simulation of $\mathrm{k}^{-5/3}$ mesoscale spectral regime in the GFDL SKYHI general circulation model. *Geophys. Res. Lett.*, **26**, 843–846.

Kunkel, B. A., 1984: Parameterization of droplet terminal velocity and extinction coefficient in fog models. *J. Appl. Meteorol.*, **23**, 34–41.

Liebe, H. J., G. A. Hufford, and T. Manabe, 1991: A model for the complex permittivity of water at frequencies below 1 THz. *Intnl. J. Infrared and Millimetre Waves*, **12**, 659–674.

Lindborg, E., 1999: Can the atmospheric kinetic energy spectrum be explained by two-dimensional turbulence? *J. Fluid. Mech.*, **388**, 259–288.

Masson, V., J.-L. Champeaux, C. Chauvin, C. Meriguet, and R. Lacaze, 2003: A global database of land surface parameters at 1 km resolution for use in meteorological and climate models. *J. Climate*, **16**, 1261–1282, doi:10.1175/1520-0442-16.9.1261.

McClatchey, R. A., R. W. Fenn, J. E. A. Selby, F. E. Volz, and J. S. Garing, 1972: Optical properties of the atmosphere. Tech. Rep. AFCRL-72-0497, Air Force Cambridge Research Laboratories, 108 pp.

McFarquhar, G. M., S. Iacobellis, and R. C. J. Somerville, 2003: SCM simulations of tropical ice clouds using observationnaly based parameterizations of microphysics. *J. Climate*, **16**, 1643–1664.

Mishchenko, M. I. and L. D. Travis, 1998: Capabilities and limitations of a current FORTRAN implementation of the T-matrix method for randomly oriented, rotationally symmetric scatterers. *J. Quant. Spectrosc. Radiat. Transfer*, **60**, 309–324.

Mishchenko, M. I., L. D. Travis, and A. A. Lacis, 2002: *Scattering, Absorption, and Emission of Light by Small Particles*. Cambridge University Press, 445 pp.

Morcrette, J.-J., 1991: Evaluation of model-generated cloudiness: satellite-observed and model-generated diurnal variability of brightness temperature. *Mon. Weather Rev.*, **119**, 1205–1224, doi:10.1175/1520-0493(1991)119%3C1205:EOMGCS%3E2.0.CO;2.

Nastrom, G. D. and K. S. Gage, 1985: A climatology of atmospheric wavenumber spectra of wind and temperature observed by commercial aircraft. *J. Atmos. Sci.*, **42**, 950–960.

Platt, C. M. R., 1973: Lidar and radiometric observations of cirrus clouds. *J. Atmos. Sci.*, **30**, 1191–1204.

Press, W. H., S. A. Teukolsky, W. T. Vetterling, and B. P. Flannery, 1992: *Numerical Recipes in FORTRAN: The Art of Scientific Computing*. 2nd Ed. Cambridge University Press, 963 pp.

Probert-Jones, J. R., 1962: The radar equation in meteorology. *Quart. J. Roy. Meteor. Soc.*, **88**, 485–495.

Pruppacher, H. R. and K. V. Beard, 1970: A wind tunnel investigation of the internal circulation and shape of water drops falling at terminal velocity in air. *Quart. J. Roy. Meteor. Soc.*, **96**, 247–256.

Rasmussen, R. M., V. Levizzani, and H. R. Pruppacher, 1984: A wind tunnel and theoretical study on the melting behavior of atmospheric ice particles. III: Experiment and theory for spherical ice particles of radius $> 500\ \mu$m. *J. Atmos. Sci.*, **41**, 381–388.

Ricard, D., C. Lac, S. Riette, R. Legrand, and A. Mary, 2013: Kinetic energy spectra characteristics of two convection-permitting limited-area models AROME and Meso-NH. *Quart. J. Roy. Meteor. Soc.*, **139**, 1327–1341, doi:10.1002/qj.2025.

Richard, E., S. Cosma, P. Tabary, J.-P. Pinty, and M. Hagen, 2003: High-resolution numerical simulations of the convective system observed in the Lago Maggiore area on 17 September 1999 (MAP IOP 2a). *Quart. J. Roy. Meteor. Soc.*, **129**, 543–563, doi:10.1256/qj.02.50.

Saunders, R., M. Matricardi, P. Brunel, S. English, P. Bauer, U. O'Keeffe, P. Francis, and P. Rayer, 2005: RTTOV-8 Science and validation report. Tech. rep., NWP SAF Rep., 41 pp.

Seliga, T. A. and V. N. Bringi, 1976: Potential use of radar differential reflectivity measurements at orthogonal polarizations for measuring precipitation. *J. Appl. Meteorol.*, **15**, 69–76.

Skamarock, W. C., 2004: Evaluating NWP models using kinetic energy spectra. *Mon. Weather Rev.*, **132**, 3019–3032.

Smith, P. L., 1984: Equivalent radar reflectivity factors for snow and ice particles. *J. Climate. Appl. Meteorol.*, **23**, 1258–1260.

Tulet, P., M. Mallet, V. Pont, J. Pelon, and A. Boone, 2008: The 7-13 March 2006 dust storm over West Africa: Generation, transport, and vertical stratification. *J. Geophys. Res.*, **113**, D00C08, doi:10.1029/2008JD009871.

van de Hulst, H. C., 1981: *Light Scattering by Small Particles*. Dover, New York, 470 pp.

Walko, R. L., W. R. Cotton, M. P. Meyers, and J. Y. J. Y. Harrington, 1995: New RAMS cloud microphysics parameterization. Part I: The single-moment scheme. *Atmos. Res.*, **38**, 29–62.

World Meteorological Organization, 2021: *Guide to Instruments and Methods of Observation, Volume I – Measurement of Meteorological Variables (WMO-No. 8)*. Geneva, URL `https://library.wmo.int/idurl/4/68695`.